Photoelectron angular distribution studies for two spin–orbit-split components of Xe 3d subshell: a critical comparison between theory and experiment

S Minemoto[1,*], T Teramoto[2], T Majima[3], T Mizuno[4], J H Mun[5], S H Park[6], S Kwon[6], A Yagishita[7,*] and D Toffoli[8]

[1] Department of Physics, Graduate School of Science, The University of Tokyo, 7-3-1 Hongo, Bunkyo-ku, Tokyo 113-0033, Japan
[2] Institute for Radiation Sciences, Osaka University, 1-1 Machikaneyama-cho, Toyonaka, Osaka 560-0043, Japan
[3] Department of Nuclear Engineering, Graduate School of Engineering, Kyoto University Uji, Kyoto 611-0011, Japan
[4] Institute for Solid State Physics, The University of Tokyo, 5-1-5 Kashiwanoha, Kashiwa, Chiba 277-8581, Japan
[5] Center for Attosecond Science and Technology, Max Planck POSTECH/KOREA Research Initiative, 77 Cheongam-Ro, Nam-gu, Pohang, Gyeongbuk 376-73, Republic of Korea
[6] PAL-XFEL, Pohang Accelerator Laboratory, 80 Jigokro-127-beongil, Nam-gu, Pohang, Gyeongbuk 376-73, Republic of Korea
[7] Institute of Materials Structure Science, KEK, 1-1 Oho, Tsukuba, Ibaraki 305-0801, Japan
[8] Dipartimento di scienze Chimiche e Farmaceutiche, Via L. Giorgieri 1, I-34127 Trieste, Italy

E-mail: minemoto@phys.s.u-tokyo.ac.jp and akira.yagishita@kek.jp

Accepted for publication 23 March 2021

Abstract

The photoelectron angular distribution asymmetry parameters β of the Xe 3d subshell were investigated using an x-ray free-electron laser (XFEL) at photon energies of 750 and 800 eV. Owing to the perfect polarization of the XFEL and two-dimensional momentum imaging capability of our velocity map imaging spectrometer, we determined the β values with high accuracy. The β values were also investigated based on relativistic time-dependent density functional theory calculations of up to 900 eV of photon energies. By comparing all the available experimental results including our data with the most reliable theories on the photon energy dependence of the β parameters, serious differences are noted between the experiments and theories. Further studies on resolving this difference will provide new insight into the photoionization processes of the deep inner shells.

Keywords: inner-shell photoionization, atomic photoionization, XFEL

1. Introduction

Photoionization studies using synchrotron radiation are a growing field of research driven by the increasing availability of advanced synchrotron radiation sources and improved theoretical methods for solving the many-electron problems occurring in atoms and molecules. This balanced account will be of value to both theorists and experimentalists working in this area. Research activities conducted by

* Authors to whom any correspondence should be addressed.

leading scientists world-wide until the mid-1990s were reviewed in an extensive monograph [1]. One can examine the graphical representations of subshell photoionization cross-sections σ and photoelectron angular distribution asymmetry parameters β of rare gas atoms, covering the photon energy range from valence ionization thresholds to 1000 eV, as provided by Becker and Shirley [2]. From the compiled graphs, it can be seen that there are no comprehensive sets within the energy range of 500–1000 eV. This situation has not improved over the past 20 years, although inner-shell processes of heavy atoms within this energy range have provided a test ground for many theoretical models and developments. Particularly in heavier systems, relativistic effects have become important [3], both for an accurate evaluation of photoionization processes and for a description of purely relativistic phenomena, such as spin–orbit splitting, the associated branching ratios, and auto-ionization resonances between fine-structure spin–orbit components.

Numerous experimental and theoretical studies on σ and β for the Xe 4d subshell have been published [1]. By contrast, to the best of our knowledge, there have been only two experimental studies on Xe 3d subshell photoionization [4, 5]. To make matters worse, experimental data are in conflict, although the near-threshold data in [5] were supported by the theoretical results [6, 7]. Thus, rational interpretations have not been given to Xe 3d subshell photoionization over the past ∼20 years. It should be noted that the spin–orbit splitting between $3d_{3/2}$ and $3d_{5/2}$ is quite large at 12.6 eV [8], and thus two relevant photo-lines can be observed separately without any experimental difficulties, which are described by the continuum eigenfunctions of the Dirac–Coulomb Hamiltonian. From this, one might think that the Xe 3d subshell photoionization experiments provide the ideal testing ground for relativistic theories.

In the present study, we report the photoelectron angular distribution asymmetry parameters β for the spin–orbit-split $3d_{3/2}$ and $3d_{5/2}$ components of Xe, using an x-ray free-electron laser (XFEL), that is, a small portion of our XFEL beam time for our project of x-ray photoelectron diffraction experiments was devoted to this fundamental subject of photoionization [9]. Owing to the perfect polarization of the XFEL [10] and the two-dimensional (2D) momentum imaging capability of our velocity map imaging spectrometer (VMI) [11], we have determined the β values with high accuracy at two photon energies of 750 and 800 eV. We also report relativistic time-dependent density functional theory (RTDDFT) calculations for the β parameters, which extend the calculations reported in [6] up to photon energies of 900 eV. Thus, the present study makes it possible to compare all the experimental results including our newly acquired data with the most reliable theory on the photon energy dependence of the photoelectron angular distribution asymmetry parameters β for the two spin–orbit-split components, over the wide energy range from the threshold to 900 eV. The remainder of this paper is organized as follows. Section 2 describes the experimental details. Section 3 provides a short explanation of our theoretical model. Section 4 compares all experimental data with the present theoretical results. Section 5 discusses the problems clarified in the present study. Finally, section 6 suggests areas for future theoretical and experimental research.

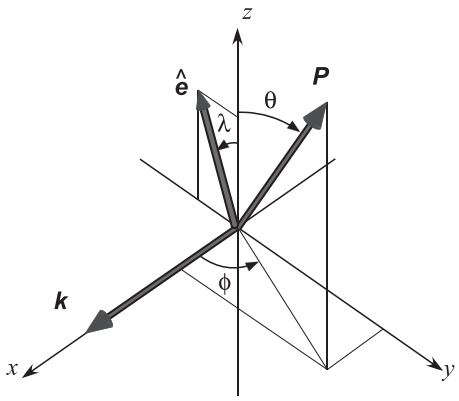

Figure 1. The coordinate system of the present experimental setup. The photon propagates along the x-axis. The polarization vector $\hat{\boldsymbol{e}}$ is on the y–z plane, the tilted angle λ of which is measured from the z-axis. The photoelectrons are emitted with the momentum $\boldsymbol{P}$, the direction of which is defined by the polar angle θ and the azimuth angle ϕ. The drift-tube axis of our VMI is along the y-axis perpendicular to the x–z plane.

2. Experiment

2.1. Experimental setup

The experiments were conducted at the SSS beamline of PAL-XFEL [12]. The experimental geometry is shown in figure 1. The drift-tube axis of our VMI is perpendicular to the x–z plane, which contains both the propagation direction ($\boldsymbol{k}$) and the polarization vector ($\hat{\boldsymbol{e}}$) of the XFEL. XFEL pulses, with an energy of ∼100 μJ pulse^{-1} and a duration of ∼50 fs, were focused using Kirkpatrick–Baez mirrors located ∼3000 mm upstream of the interaction region. The size and position of the focused XFEL beam were monitored using a Ce:YAG screen inserted in the VMI chamber. The typical spot size was ∼60 μm in the y-direction and ∼80 μm in the z-direction. The typical bandwidth of an XFEL is ∼0.5%, that is, ∼4 eV at a photon energy of 750 eV [12]. The sCMOS camera of the VMI was synchronized with the XFEL pulses at a repetition rate of 30 Hz.

A pulsed supersonic atomic beam of the VMI was formed by expanding a pure 4 bar Xe gas through the 100 μm-diameter aperture of the pulsed valve developed by Even *et al* [13] into a vacuum chamber. The atomic beam through a 3 mm diameter skimmer was introduced into the interaction region with the XFEL beam. The source and main chambers were differentially pumped by turbo-molecular pumps and their typical pressures during the experiments were 1×10^{-4} and 3×10^{-6} Pa, respectively. The pulse duration of the valve was controlled at between 21 and 22 μs by monitoring the pressure of the source chamber. The timing and duration of the valve were optimized by monitoring Xe ion signals from the ion time-of-flight (TOF) drift tube of the VMI. The pulsed valve was operated at a repetition rate of 15 Hz.

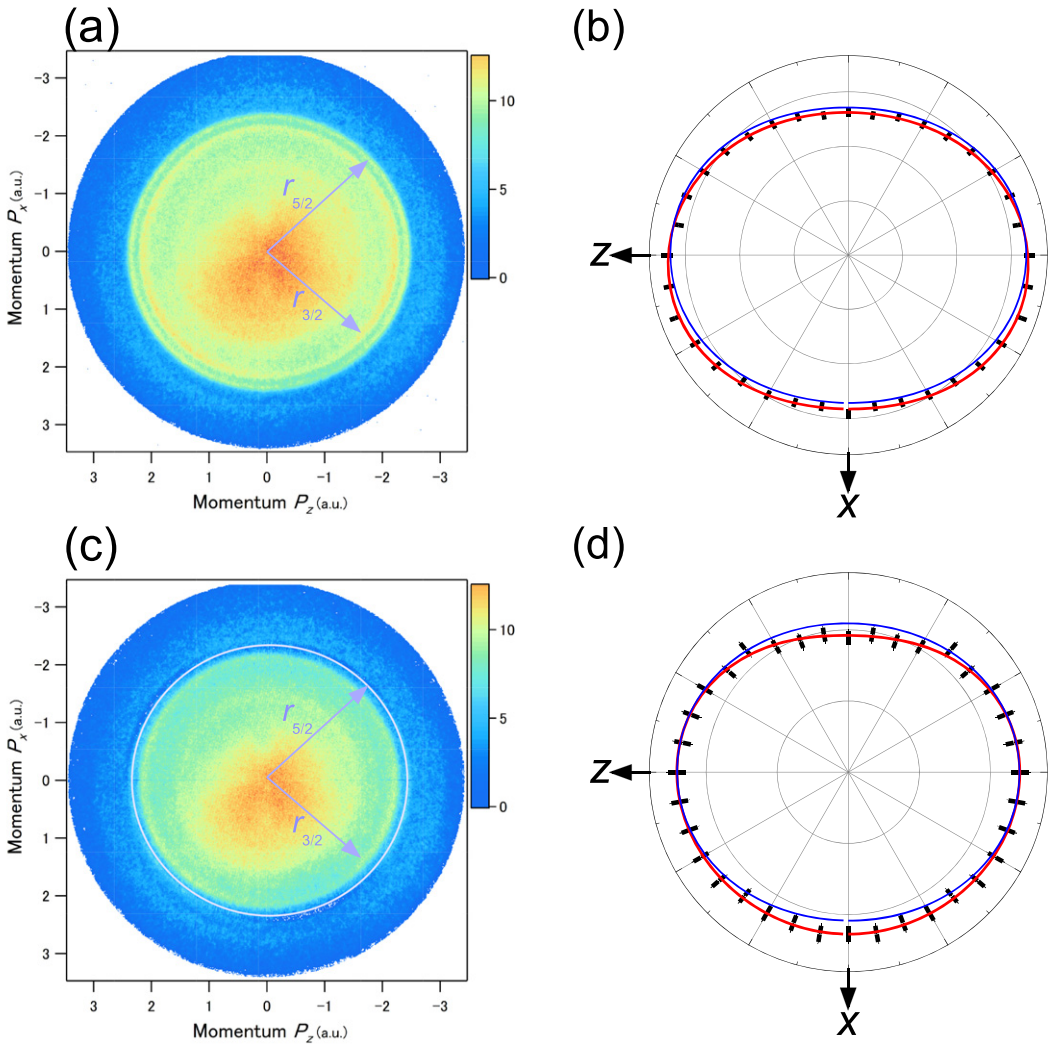

Figure 2. 2D photoelectron images for $Xe3d_{5/2}$ (a) and $Xe3d_{3/2}$ (c) and polar plots for $Xe3d_{5/2}$ (b) and $3d_{3/2}$ (d). In (a), the rings corresponding to the Xe $3d_{5/2}$ and $3d_{3/2}$ photoionization are clearly observed at the radii of $r_{5/2} = 2.38$ and $r_{3/2} = 2.15$ a.u., respectively. In (b), the experimental results are plotted by solid bars, the lengths of which show the statistical errors. The bold solid curve is the fitted result of equation (1). The thin solid curve is the fitted result of equation (1) with $\gamma = 0$ and $\delta = 0$. In (c), the $3d_{5/2}$ photoionization contributions are subtracted from the 2D image of (a). In (d), the experimental results are plotted by solid bars. The bold solid curve is the fitted result when considering the nondipolar effects. The thin solid curve is the fitted results within the dipole approximation. In (a) and (c), continuous low-lying electrons owing to shake-off processes and Auger electrons are observed.

In the VMI, velocity-focused photoelectrons were detected using a chevron-stacked dual microchannel plate (MCP) backed by a phosphor screen [11, 14]. The MCP was gated by applying a pulsed voltage of 300 V at the front for a duration of 1 μs. By gating the MCP, the false electron signals originating from the surface of the MCP for ion detection [15] can be removed. The image on the phosphor screen was recorded shot-by-shot using an sCMOS camera and stored in a PC. The photoelectron 2D momentum images with and without the sample atoms were alternately measured, and the objective images from only the sample gas were then obtained by subtracting the latter from the former. We acquired momentum image data between 5000 and 30 000 shots of XFEL pulses.

2.2. Data analysis

Figure 2(a) shows a 2D momentum image of the Xe 3d photoelectrons at an XFEL photon energy of 750 eV. The two rings for the photoionization of the Xe $3d_{5/2}$ and $3d_{3/2}$ subshells are clearly separated with radii of $r_{5/2} = 2.38$ and $r_{3/2} = 2.15$ a.u. Inside the rings, low-energy electrons owing to photoelectron and Auger electron shake-off processes are observed, which are shifted from the center of the image by residual magnetic fields. However, these electrons did not affect the analysis of the Xe 3d photoelectrons. The signal intensities of the inner ring, $r_{3/2} = 2.15$ a.u., for Xe $3d_{3/2}$ photoionization are superimposed on those of the outer ring,

$r_{5/2} = 2.38$ a.u., for Xe $3d_{5/2}$. Thus, we started analyses of the outer ring for Xe $3d_{5/2}$: the ring was divided into 36 sectors with $\Delta\theta = 10°$. Then, the radial distribution for each sector was created by integrating the signals over $\Delta\theta = 10°$. Each radial distribution at $\geqslant r = 2.18$ a.u. was least-squares-fitted using an asymmetric Gaussian function, the center of which was fixed to $r_{5/2} = 2.38$ a.u. with widths of 0.30 and 0.40 a.u. for the higher and lower momentum sides, respectively. From this procedure, we obtained a polar angle θ distribution of photoelectrons for the Xe $3d_{5/2}$ subshell, which is shown in figure 2(b).

Under conditions by which the first-order corrections to the dipole approximation satisfy the following requirements, i.e. the corrections to the dipole approximation arising from the E1 and E2 and E1–M1 interference terms are accounted for through the introduction of two independent angular distribution parameters γ (E1–E2) and δ (E1–M1) [16–18], the photoelectron angular distribution in our experimental geometry shown in figure 1 is written as follows [19]:

$$\begin{aligned}\frac{d\sigma}{d\Omega}(\tilde{S}_1, \lambda) = \frac{\sigma}{4\pi}\Bigg\{&\left[1 + \frac{\beta}{8}\left(1 + 3\tilde{S}_1\ \cos\ 2\lambda\right)\left(3\cos^2\theta - 1\right)\right] \\ &+ \left[\delta + \gamma\cos^2\theta + \frac{\gamma}{8}\left(\tilde{S}_1\ \cos\ 2\lambda - 1\right)\right. \\ &\left.\times\ \left(5\cos^2\theta - 1\right)\sin\ \theta\ \cos\ \phi\right] \\ &+ \left[\frac{3\beta}{8}\left(\tilde{S}_1\ \cos\ 2\lambda - 1\right)\right]\sin^2\theta\ \cos\ 2\phi \\ &+ \left[\frac{\lambda}{8}\left(\tilde{S}_1\ \cos\ 2\lambda - 1\right)\right]\sin^3\theta\ \cos\ 3\phi\Bigg\}, \qquad (1)\end{aligned}$$

where $\tilde{S}_1$ is defined as the greatest possible value of the Stokes parameter for linear polarization, and λ is the tilt angle of the major polarization ellipse relative to the z axis, which implies $\tilde{S}_2 = 0$. In the present case, $\phi = 0$ or π because the photoelectrons were measured in the x–z plane. Nondipolar effects manifest themselves through backward/forward anisotropies along the photon momentum $\boldsymbol{k}$. These can be forward-directed for positive values of γ and δ, or backward-directed for negative values of the parameters. The fitting of the least-squares case of equation (1) to the experimental data is shown in figure 2(b). The relevant fitted parameters are summarized as follows: $\beta = 0.128 \pm 0.037$, $\delta = 0.04 \pm 0.03$, $\gamma = 0.01 \pm 0.04$, and $\tilde{S}_1\ \cos\ 2\lambda = 1.00^{+0.00}_{-0.07}$. The value of $\tilde{S}_1\ \cos\ 2\lambda = 1.00^{+0.00}_{-0.07}$ (i.e. $\tilde{S}_1 = 1$ and $\lambda = 0°$) agrees perfectly with the degree of polarization of the SASE-XFEL estimated from [10]; for SASE-XFEL at PAL-XFEL, it can be seen that the horizontal polarized component (e_z) of radiation significantly dominates the photon beam characteristics, and an intensity of only less than 1.8 out of a total of one million is polarized along the y–z vertical plane. This value can be calculated from the equation of $\lambda_w^2/(4\pi L_g)^2$ in [10], where λ_w is the length of the undulator period and L_g is the gain length. Owing to the positive value of $\delta = 0.04 \pm 0.03$, one can see a slightly forward-directed anisotropy in figure 2(b). However, these quite small values for the nondipole parameters γ and δ, which are consistent with the theoretical calculations for Xe 3d photoelectrons [20], have little effect on the asymmetry parameter β. By setting $\gamma = 0$ and $\delta = 0$, we fitted equation (1) to the experimental data and obtained the results of $\beta = 0.129 \pm 0.042$. This fitted curve is shown in figure 2(b). It is noteworthy that the appearance of backward/forward anisotropies is sensitive in the case of $\beta \sim 0$, as in the present experiment, and insensitive in the case of $\beta \sim 2$, e.g. in [21], because in the former case the photoelectron intensity is appreciable in the backward/forward directions, whereas in the latter case it is significantly suppressed.

To determine the asymmetry parameter β for the Xe $3d_{3/2}$ subshell, the contributions of the photoelectrons from the Xe $3d_{5/2}$ subshell, which are reproduced using the determined asymmetry parameter β and asymmetric radial distribution function, were subtracted from the measured 2D image shown in figure 2(a). This data processing is similar to the so-called peeling method [22, 23], which is applicable to cylindrically symmetric angular distributions. However, the cylindrical symmetry can be broken in the present case by the backward/forward anisotropies due to the nondipole effects, and thus we did not adopt the peeling method. The resultant 2D image is shown in figure 2(c). The procedure used to create a polar plot from this 2D image is the same as that for the Xe $3d_{5/2}$ subshell. The only difference between them is the integration area, where the radius was fixed to $r_{3/2} = 2.15$ a.u. and the widths are 0.28 and 0.36 a.u. for the higher and lower momentum sides, respectively. The polar plot of the photoelectron angular distribution for the Xe $3d_{3/2}$ subshell is shown in figure 2(d). The fitting of the least-squares curve of equation (1) to the experimental data is shown in figure 2(d). The relevant fitted parameters are summarized as follows: $\beta = 0.099 \pm 0.054$, $\delta = 0.07 \pm 0.06$, $\gamma = -0.06 \pm 0.04$, and $\tilde{S}_1\ \cos\ 2\lambda = 1.00^{+0.00}_{-0.10}$. By setting $\gamma = 0$ and $\delta = 0$, we fitted equation (1) to the experimental data, and obtained the results of $\beta = 0.098 \pm 0.063$. From the results, it can be seen that the small values for the nondipole parameters have little effect on the asymmetry parameter β. The fitted curve is shown in figure 2(d). We repeated these measurements three times under different accumulation times. For one measurement, we adopted the pulse-gated mode for the MCP, and for the other two we did not. We then confirmed that the magnitudes of asymmetry parameter β did not depend on both the accumulation times and the measurement modes. Thus, we took an average of the three values determined for the asymmetry parameter β, which are shown in figure 3.

At an XFEL photon energy of 800 eV, we repeated the measurements and data processing procedure mentioned here, and obtained the following results: $\beta = 0.203 \pm 0.020$ for $3d_{5/2}$ and $\beta = 0.108 \pm 0.054$ for $3d_{3/2}$.

3. Calculations

The partial cross-sections σ and asymmetry parameters β for the spin–orbit-split $3d_{5/2}$ and $3d_{3/2}$ components of Xe, from the threshold up to a photon energy of 900 eV, are calculated using the RTDDFT method implemented in an atomic B-spline code [6]. An account of the implementation has

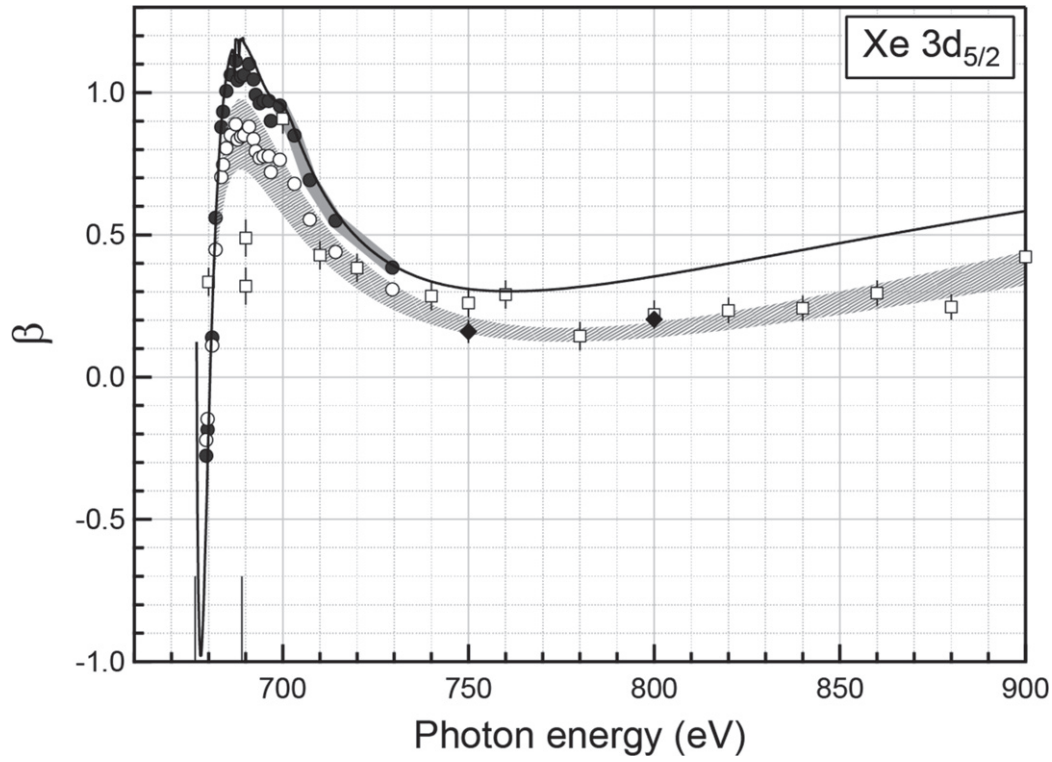

Figure 3. The photoelectron angular distribution asymmetry parameters β for the $3d_{5/2}$ subshell photoionization of Xe. Filled diamonds, present results; open squares, Becker *et al* [4]; filled circles, Kivimäki *et al* [5]; open circles, corrected data of Kivimäki *et al* [5], which are multiplied by 0.8, see text. The bold curve is the present RTDDFT. The shaded band denotes the average of the three data sets of the diamonds, squares, and open circles. The width of the band is ±15% of the values. The vertical lines on the abscissa indicate the ionization energies of the Xe $3d_{5/2}$ and $3d_{3/2}$ subshells.

been given before [6]; therefore, we summarize only the more important equations and provide a description of the parameters that define the B-spline basis. We first solve the set of relativistic Kohn–Sham (KS) equations, by using the LB94 [24] exchange–correlation potential, which provides occupied orbitals φ_i and eigen-energies ε_i. The first-order perturbations on the Dirac–Kohn–Sham eigen-functions, and the self-consistent induced field, $v^{\mathrm{SCF}}(\boldsymbol{r},\omega)$, are then calculated from the following coupled equations, according to first-order perturbation theory, and within the adiabatic local density approximation:

$$[h_{\mathrm{D}} - \varepsilon_i \pm \omega]\,\varphi_i^{(1,\pm)} = P v^{\mathrm{SCF}} \varphi_i, \tag{2}$$

$$v^{\mathrm{SCF}}(\boldsymbol{r},\omega) = v^{\mathrm{ext}}(\boldsymbol{r},\omega) + \int \frac{\delta\rho(\boldsymbol{r}',\omega)}{|\boldsymbol{r}-\boldsymbol{r}'|}\,d\boldsymbol{r}' + \left(\frac{\partial v_{xc}}{\partial \rho}\right)_{\rho_{gs}} \delta\rho(\boldsymbol{r},\omega). \tag{3}$$

In equation (2), h_{D} is the relativistic Dirac KS Hamiltonian, ω is the photon energy, and the projection operator P orthogonalizes with respect to the occupied KS states, whereas v^{ext} is the external dipole potential. The first-order induced density, $\delta\rho(\boldsymbol{r},\omega)$, is calculated from $\varphi_i^{(1,\pm)}$ according to the following equation:

$$\delta\rho(\boldsymbol{r},\pm\omega) = \sum_i n_i \left[\varphi_i^{\dagger}\varphi_i^{(1,\pm)} + \varphi_i \varphi_i^{(1,\mp)\dagger}\right]. \tag{4}$$

The electric dipole differential cross-section for the ionization from the subshell $(n\kappa)$ can be written as

$$\frac{d\sigma_{n\kappa}}{d\Omega} = \frac{\sigma_{n\kappa}(\omega)}{4\pi}\left[1 - \frac{1}{2}\beta_{n\kappa}(\omega) P_2(\cos\,\theta)\right], \tag{5}$$

in terms of the partial cross-section $\sigma_{n\kappa}$ and the asymmetry parameter $\beta_{n\kappa}$, which are expressed in terms of the phase shifts and dipole matrix elements as follows [25]:

$$\sigma_{n\kappa}(\omega) = \frac{4\pi^2\,\alpha}{3}\omega\left(|D_{j\to j-1}|^2 + |D_{j\to j}|^2 + |D_{j\to j+1}|^2\right), \tag{6}$$

and

$$\begin{aligned}\beta_{n\kappa}(\omega) = \Bigg[&\frac{1}{2}\frac{(2j-3)}{2j}|D_{j\to j-1}|^2 - \frac{3}{2j}\left(\frac{2j-1}{2\,(2j+2)}\right)^{\frac{1}{2}} \\ &\times \left(D_{j\to j-1}D^*_{j\to j} + \text{c.c.}\right) - \frac{(2j-1)\,(2j+3)}{(2j)\,(2j+2)} \\ &\times |D_{j\to j}|^2 - \frac{3}{2}\left(\frac{(2j-1)(2j+3)}{2j(2j+2)}\right)^{\frac{1}{2}} \\ &\times \left(D_{j\to j-1}D^*_{j\to j+1} + \text{c.c.}\right) + \frac{1}{2}\frac{(2j+5)}{(2j+2)} \\ &\times |D_{j\to j+1}|^2 + \frac{3}{(2J+2)}\left(\frac{2j+3}{2(2j)}\right)^{\frac{1}{2}}\end{aligned}$$

$$\times \left(D_{j\to j} D^{*}_{j\to j+1} + \text{c.c.}\right)\Big] \times \left(|D_{j\to j-1}|^2 + |D_{j\to j}|^2 + |D_{j\to j+1}|^2\right)^{-1}. \quad (7)$$

Here, the term $D_{j\to j-1}$ is absent for $j = 1/2$. The dipole matrix elements $D_{j\to\bar{j}}$ between the initial state $a \equiv (n\kappa)$ and the final energy normalized state $\bar{a} \equiv (E\bar{\kappa})$ appearing in equations (6) and (7) can be written in terms of a reduced dipole matrix element multiplied by a factor containing the partial-wave phase shifts $\delta_{\bar{\kappa}}$:

$$D_{j\to\bar{j}} = i^{1-\bar{\ell}}\, e^{i\delta_{\bar{\kappa}}} \left\langle \bar{a}\|Q_1^{(1)}\|a \right\rangle, \quad (8)$$

where

$$\left\langle \bar{a}\|Q_1^{(1)}\|a \right\rangle = (-1)^{j+1/2}[\bar{j}][j] \begin{pmatrix} j & \bar{j} & 1 \\ -1 & 1 & 0 \\ \hline 2 & 2 & \end{pmatrix} \pi(\bar{\ell}, \ell, 1) \times R_1^1(\bar{a}, a). \quad (9)$$

In equation (9), $[j] = (2j+1)^{1/2}$, π is the usual parity factor, and $R_1^1(\bar{a}, a)$ is the radial dipole matrix element, which contains $v^{\text{SCF}}(r)$ in place of the dipole operator r. The B-spline basis set used in the calculations is of order 10, and is defined on a radial grid extending up to 25.0 a.u., which is constructed as detailed in the study by Fisher and Parpia [26]. Experimental threshold energies were employed in the calculations, and all dipole channels allowed were included in the calculation. With this setup, we were able to reproduce low-energy region data published in [6], while extending the upper photon energy limit up to 900 eV. The inclusion of the experimental threshold energies in our RTDDFT equations should implicitly include some two-electron two-hole excitations in the final ionized states. However, orbital relaxation effects following a core–hole formation are not explicitly included in the computational approach.

4. Results

4.1. Asymmetry parameters β of the Xe $3d_{5/2}$ subshell

The asymmetry parameters β for the $3d_{5/2}$ subshell photoionization of Xe are shown in figure 3 together with the relevant data by Becker *et al* [4] and by Kivimäki *et al* [5]. The present RTDDFT results are also shown for comparison. On the one hand, the former determined the β parameters over a wide energy range of up to 1000 eV from the $3d_{5/2}$ photoelectron angular distributions in the dipole plane using an angle-resolved TOF spectrometer. On the other hand, the latter measured the β parameters within the near-threshold region of below 730 eV from the $3d_{5/2}$ photoelectron intensity ratios for two different angles, in principle, using a cylindrical mirror analyzer (CMA) with eight segment anodes, which was set up under the backscattering geometry. The four data points of [4] below 700 eV are strongly scattered, which may be due to contaminations of the $3d_{5/2}$ photo-lines by shake-off and/or NOO Auger electrons. Except for these data, the results of [4] are consistent with the present data; the average of them, in which the present data are weighted, is shown by a shaded band. The deviation of the average values from the RTDDFT results at 710 eV is gradually increasing toward the high energy side. In contrast to this, the data of [5] below 730 eV agree with the RTDDFT results. From these observations, one can notice a gap between the experimental data of [5] and the average values of [4] and the present measurement in the overlap region from 710 and 730 eV (see figure 3), as mentioned in the introduction section 1. However, this gap was overlooked until the present work, because in [5] the preceding β parameter results of [4] was not referred to at all. As a natural consequence of this, it has been believed for a long time, since the early 2000s, that the data in [5] below 730 eV are well reproduced by the relativistic theories [5–7].

This gap might be considered due to large systematic errors relevant to the experimental procedure of [5], the possible issues of which are interpreted as follows. Kivimäki *et al* [5] measured the photoelectron intensities with both one anode parallel to the synchrotron ring plane and the other anode perpendicular to the plane, and calculated the β values from their ratios 'without definite characterizations on the polarization of the synchrotron radiation applied'. Hence one can say that their approach is inadequate, because the photoelectron angular distributions in their geometry is expressed by (see equation (1.53a) in [27])

$$\frac{d\sigma}{d\Omega}(\tilde{S}_1, \lambda) = \frac{\sigma}{4\pi}\left[1 + \frac{\beta}{2}\tilde{S}_1 \cos 2(\phi - \lambda)\right], \quad (10)$$

where the definitions of the polarization parameters of $(\tilde{S}_1, \lambda)$ are the same as equation (1). As can be seen in equation (10), to determine the β values one must determine the polarization parameters at first. In spite of this they skipped this procedure, and then just assuming $\lambda = 0°$ got $\tilde{S}_1 = 0.7$ from the calibration data for Ne 2s photo-line. Owing to their rough procedure, the magnitudes of their β values must include large systematic errors, which might be estimated as roughly 30%, although the photon energy dependence of their β values can be preserved. The ∼30% uncertainties can be evaluated by changing from $\lambda = 0°$ to $\lambda = 20°$ in equation (10), under the condition of the 45° acceptance angle for their each segment detector. To remove the long-standing discrepancies mentioned in the previous paragraph, we multiplied their β values by 0.8 in such a way that the gap between the two datasets disappears, which is shown by a shaded band in figure 3.

It should be noted that Kivimäki *et al* [5] reported that their experimental β values for the $3d_{5/2}$ subshell photoionization of Xe within the near-threshold region are reproduced well by their relaxed single-channel calculations based on relativistic theory. Later, Toffoli *et al* [6] and Radojević *et al* [7] published the theoretical β values, which agree with the experimental β values. However, we should state that such agreements were caused by an accident because the magnitudes of the experimental β values have large uncertainties, as mentioned above. In fact, as can be seen from figure 3, in which the corrected data are plotted, there are noticeable differences in the magnitudes of the β values between the theory and experiment. However, from the present work, it is found that except for differences in the magnitude, the RTDDFT results reproduce the overall trend of the photon energy dependence over the entire energy range from the threshold to 900 eV. It should be noted that

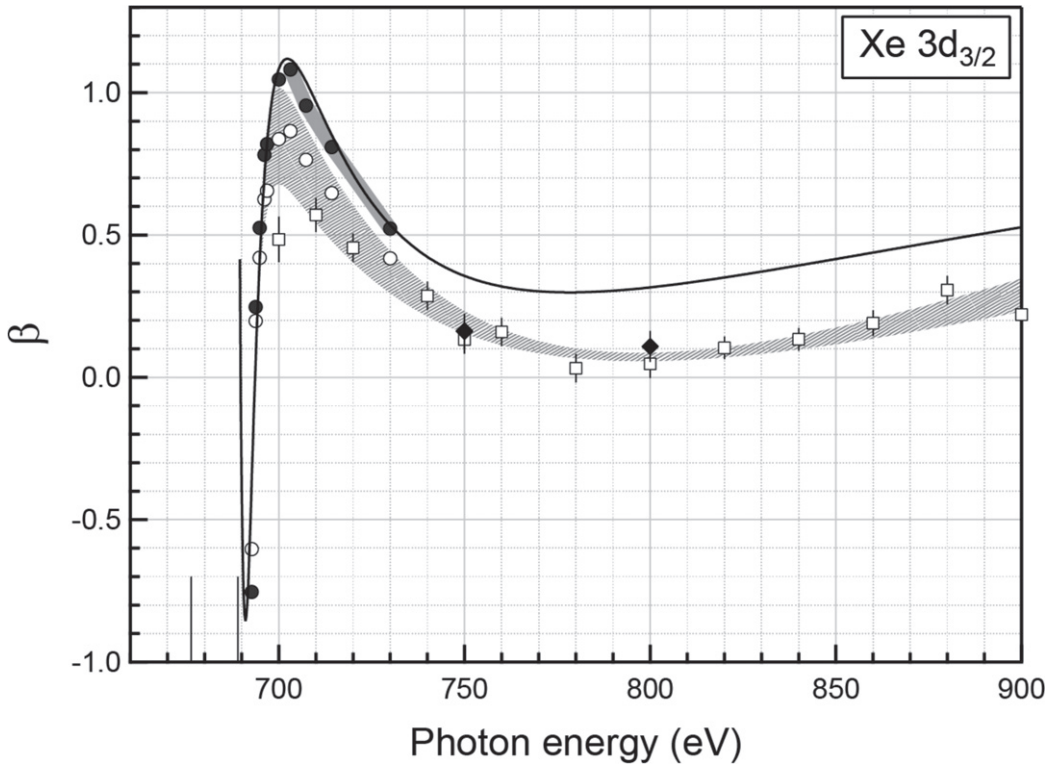

Figure 4. The photoelectron angular distribution asymmetry parameters β for the $3d_{3/2}$ subshell photoionization of Xe. Filled diamonds, present results; open squares, Becker *et al* [4]; filled circles, Kivimäki *et al* [5]; open circles, corrected data of Kivimäki *et al* [5], which are multiplied by 0.8, see text. The bold curve is the present RTDDFT. The shaded band denotes the average of the three data sets of the diamonds, squares, and open circles. The width of the band is $\pm$20% of the values. The vertical lines on the abscissa indicate the ionization energies of the Xe $3d_{5/2}$ and $3d_{3/2}$ subshells.

the tiny shoulder structure at ~700 eV observed in both the theory and experiment might be due to the interchannel coupling between the two 3d ionization continua. A detailed comparison between the present results and all available theories are discussed in section 5, where we intensively refer to asymmetry parameters only, as the situation for cross-sections is better.

4.2. Asymmetry parameters β of the Xe $3d_{3/2}$ subshell

The asymmetry parameters β for the $3d_{3/2}$ subshell photoionization of Xe are shown in figure 4 along with the relevant data by Becker *et al* [4] and Kivimäki *et al* [5]. The present RTDDFT results are also shown for comparison. The corrected β values of [5], which were multiplied by 0.8, are also shown for the same reason described in the previous section 4.1. As can be seen from figure 4, the corrected data of [5] are smoothly connected to the average values of [4] and the present by a shaded band. From these observations, for the β values of the $3d_{3/2}$ subshell photoionization of Xe within the near-threshold region, the same scenario as the $3d_{5/2}$ subshell photoionization is applicable, that is, the agreement between the experiment [5] and the three relativistic theories [5–7] is not real, but is apparent. In fact, there are clear differences in the magnitudes of the β values between the theory and the experimental average values expressed by the shaded band, although the RTDDFT results reproduce their photon energy dependence over a wide energy range from the threshold to 900 eV. Further discussions are given in section 5.

Although the asymmetry parameters β are expressed by the photon energy scale in figures 3 and 4, it is interesting to express them by the photoelectron energy scale. This can be achieved by shifting figure 4 to the low-energy side by 12.6 eV. In comparing figure 3 with figure 4, shifted by 12.6 eV, the photoelectron energy dependence of the asymmetry parameters β by the RTDDFT are extremely similar for the $3d_{5/2}$ and $3d_{3/2}$ subshells. The position of the shallow minimum for $3d_{5/2}$ and $3d_{3/2}$ is at a photoelectron energy of 85 eV. The experimental results also exhibit a shallow minimum at ~85 eV. This implies that the photoionization dynamics for the two spin–orbit-split components of the Xe 3d subshell are similar.

5. Discussion

A compilation of the asymmetry parameters β for the $3d_{5/2}$ subshell obtained in different approximations [5, 28–30] is shown in figure 5 along with the experimental values assessed in the previous section and the present RTDDFT results. All theoretical binding energies of the $3d_{5/2}$ subshell were adapted to the experimental ionization energy. The β values calculated by the relativistic random phase approximation (RRPA) by Kutzner *et al* [29] are cross-section averaged values for $\beta_{3d_{5/2}}$ and $\beta_{3d_{3/2}}$. The maximum photon energy at approximately 690 eV is mostly produced by the $3d \rightarrow \varepsilon f$ shape resonance

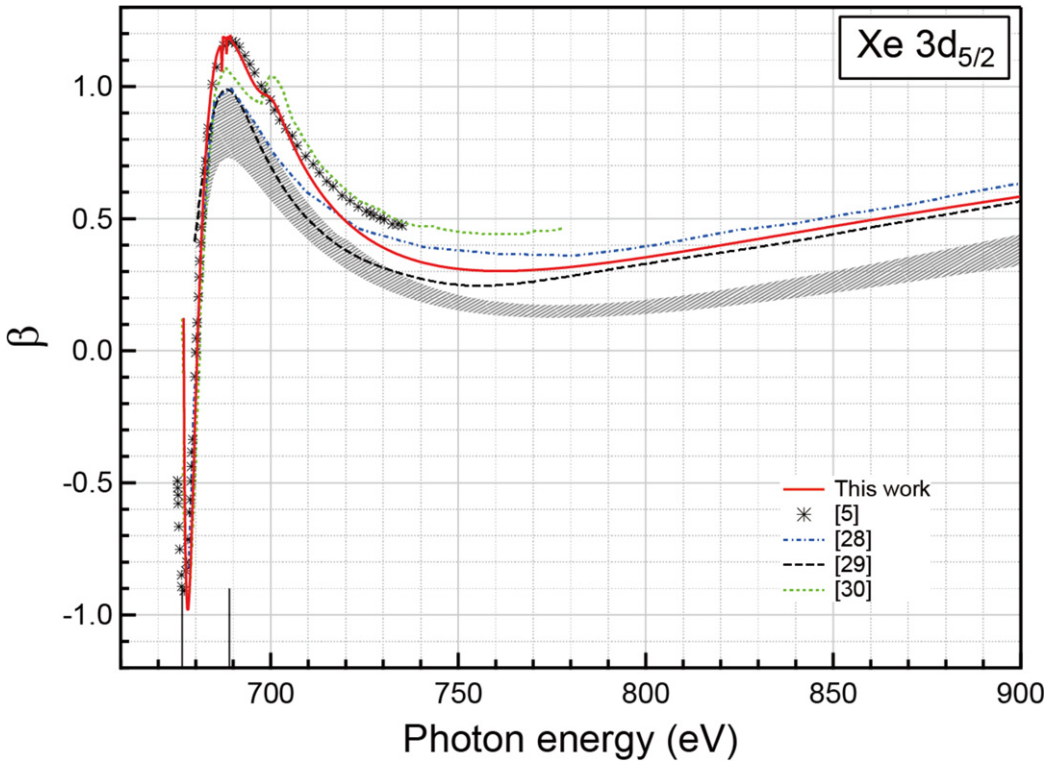

Figure 5. A compilation of the asymmetry parameters β for the Xe $3d_{5/2}$ subshells theoretically obtained in different approximations, the references of which are written in the inset. The shaded band denotes the average experimental data, which are the same as in figure 3.

effect [31]. The shoulder within the vicinity of 700 eV owing to the interchannel interaction is reproduced by the present RTDDFT and by the spin-polarized RPAE [30]. For higher energies, the β values are a smooth function of the photon energy with a shallow minimum at approximately 760 eV, which is in contrast to the deep minimum of the β values for the 4d subshell photoionization owing to the Cooper minimum [6, 32, 33]. Related to this, using the present RTDDFT, the $3d_{5/2}$ subshell photoionization cross-section, which is not shown here, monotonically decreases for higher energies and does not show the presence of a Cooper minimum.

A comparison of the experimental data with the results from the different theoretical approaches in figure 5 shows that all theories reproduce the general shape of the asymmetry parameter β as a function of the photon energy, although in the 3d partial photoionization cross-sections, both the Hartree–Fock (HF) [28] and RRPA [29] results exhibit two extremely narrow peaks that are considerably higher and narrower than the peaks seen in the measured cross-sections [4, 5, 34]. This is a consequence of some cancellation effects in the correct magnitude of the matrix elements involved because they appear in the expression for β, not only in the numerator, but also in the denominator, as indicated in equation (7). The differences between theory and experiment can be found in the magnitude of the β values. In fact, the RTDDFT calculations are in excellent agreement with the experimental data over the entire energy range from the threshold to 900 eV, if the theoretical results are multiplied by $\sim$(0.7–0.8).

Far above the shape resonance at a photon energy of approximately 690 eV, the photoemission process seems to be simple. Indeed, the HF calculations reproduce the experimental 3d partial photoionization cross-sections [4, 34]. It is therefore interesting to compare the results from the different theoretical approaches within a higher energy region than 750 eV. In figure 5 the two relativistic calculations of the present RTDDFT and RRPA [29] show close values of the β parameters. The HF calculations [28] are also similar to the two relativistic calculations, although they deviate from the experimental data to the largest extent. Thus, from these comparisons we cannot state that the relativistic effects appear in the differences between the relativistic and non-relativistic theories. To reproduce the experimental results, correlations in the bound states and satellite excitation must be included in the approximation for both non-relativistic and relativistic theories.

A compilation of the asymmetry parameters β for the $3d_{3/2}$ subshell obtained in different approximations [5, 28–30] is shown in figure 6 along with the experimental values assessed in the previous section and the present RTDDFT. All the theoretical binding energies of the $3d_{3/2}$ subshell were adapted to the experimental ionization energy. The HF [28] and RRPA [29] results are the same as those in figure 5, although their binding energies are shifted from the $3d_{5/2}$ to $3d_{3/2}$ ionization energy. As discussed in section 4, the photoelectron energy dependence of the asymmetry parameters β for $3d_{3/2}$ is very similar to that for $3d_{5/2}$, as shown in figures 5 and 6, and thus all descriptions of the theoretical results and a comparison of the theory and experiment for the asymmetry parameters β

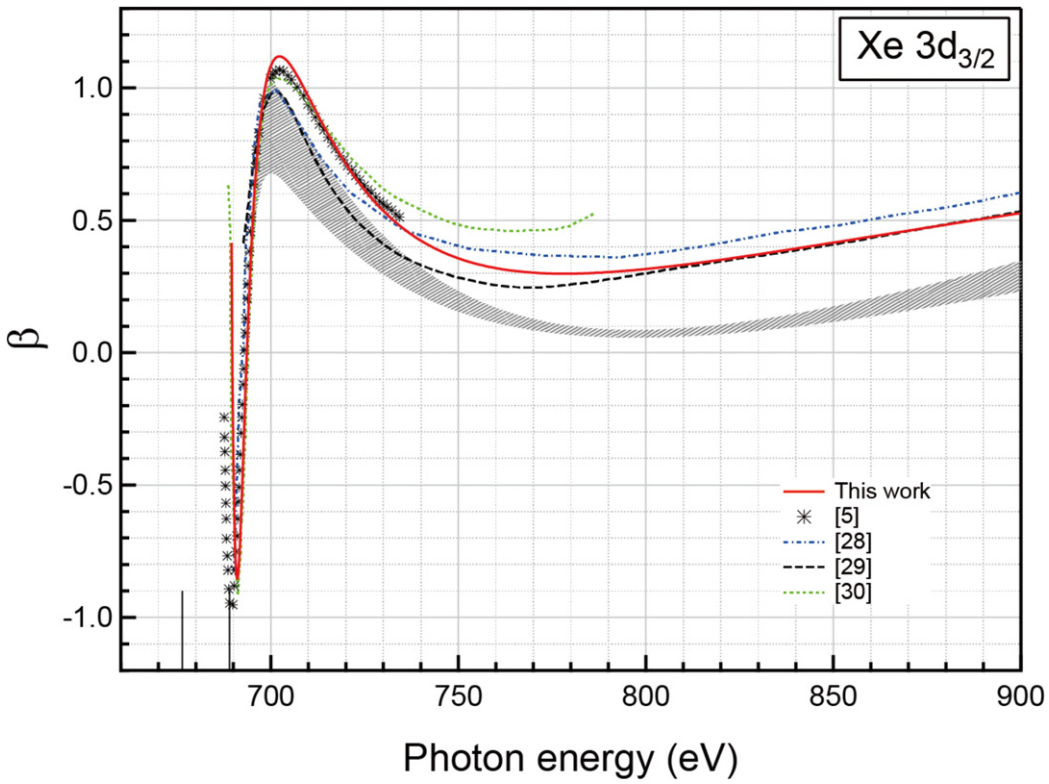

Figure 6. A compilation of the asymmetry parameters β for the Xe $3d_{3/2}$ subshells theoretically obtained in different approximations, the references of which are written in the inset. The shaded band denotes the average experimental data, which are the same as in figure 4.

of $3d_{5/2}$ mentioned in the previous paragraphs are applicable to the discussions about those for $3d_{3/2}$. The only difference between them is the magnitude near the shallow minimum of the experimental asymmetry parameter β. That is, at above 750 eV, the discrepancy between the theory and experiment in terms of the magnitudes of the asymmetry parameters β for $3d_{3/2}$ is larger than that for $3d_{5/2}$. In other words, at above 750 eV, the magnitudes of the experimental β for $3d_{3/2}$ are slightly smaller than those for $3d_{5/2}$.

At the end of this section, we refer to reliability of the experimental photoionization cross-sections σ of the 3d subshells of [5], which were well reproduced by their relativistic theory. Later on, their cross-sections data were supported by the theoretical works of [6, 7]. This was believed for a long time, like the above mentioned scenario on the β parameters. However, here we point out that the experimental values of cross-sections σ of [5] are overestimated by the following reasons. In their backscattering geometry setup of the CMA, in other words, in the nondipole magic angle CMA, the photoelectron peak intensities are independent of the β parameter, but not proportional to the partial photoionization cross-section owing to forward and backward anisotropies induced by the nondipole effect [5, 16, 35] (also see the appendix). Based on the correction described in the appendix, the reported experimental cross-section values should be multiplied by 0.86. As a consequence of this correction, the relativistic theoretical results of [5, 6] without core–hole relaxation effects become ∼15% higher than the experimental values. This type of difference in the partial cross-section between the theory and experiment is well known for the Xe 4d subshell photoionization cross-sections; the relativistic theories that do not include core–hole relaxations overestimate the cross-section by ∼25% [1, 6, 29, 33, 34]. Thus, we can summarize that the degree of difference changes from ∼25% for the 4d subshell to ∼15% for the 3d shell. This is qualitatively understandable, as the result of the different strength of the relaxation effect, if one takes the lifetimes of the relevant core–hole into account, i.e. 6.5 fs for Xe 4d and 1 fs for Xe 3d [36].

6. Concluding remarks

As mentioned in the introduction, there are no comprehensive sets of both photoionization cross-sections σ and photoelectron angular distribution asymmetry parameters β of rare gas atoms within the energy range of between 500 and 1000 eV, although the inner-shell processes of heavy atoms in this energy range provide a testing ground for many theoretical models and developments. Thus, we studied the photoionization of the Xe 3d subshell using a sophisticated theoretical method and experimental tools. In particular, we focused on the asymmetry parameters β for the two spin–orbit-split components of the Xe 3d subshell, because the situation for the cross-section is better. As a result, in contrast to the general understanding of the photoionization dynamics, which is well described by the independent-particle approximation for higher photon energies, we noticed some serious differences between the theory and experiment in terms of the magnitudes of the asymmetry parameters β for the spin–orbit-split

components of the Xe 3d subshell at above 750 eV. It was found that both relativistic and interchannel coupling effects play an important role in accurately describing the ionization dynamics of the 3d photoelectrons. The results of an independent particle approximation, exemplified by the relativistic KS approach, are unable to describe the near-threshold spin–orbit activated interchannel coupling between the 3d main lines, which is visible as weak modulations in the $3d_{3/2}$ partial cross-section and asymmetry parameter profile. The inclusion of interchannel coupling among all main-line channels was shown to generally improve the agreement between the theoretical and experimental β values over all photon energy intervals investigated. Surprisingly, however, the lack of a perfect agreement between RTDDFT estimates and the measured β values would suggest that additional initial and final state effects, together with the coupling of additional dipole channels (i.e. photoionization with excitation channels) are needed to obtain a quantitative agreement between theory and experiment. In principle, the initial and final state effects can be accurately included through the use of Dyson orbitals, which could be coupled with the multichannel TDDFT approach. This could represent a viable approach beyond TDDFT, with potential application in atomic and molecular systems, for which a full close-coupling expansion of the scattering wave function would prove computationally prohibitive. Studies along these lines are planned for the near future.

To the best of our knowledge, the present study is the first sophisticated theoretical and experimental consideration of the fundamental photoionization process of the deep inner shell of a heavy atom. Further experimental and theoretical studies are required to resolve the problem of the serious differences incurred, and will provide new insight into the fundamental interpretation of the photoionization of a deep inner shell.

Acknowledgments

The authors thank the staff members of PAL-XFEL, particularly Dr. S Rah, for their support with the XFEL experiments, which were conducted at the SSS beamline of PAL-XFEL with the approval of PAL (Proposal No. 2019-1st-SSS-007). AY and DT thank Professor P Decleva for his valuable discussions on the theoretical results. This research was supported by the Bilateral Joint Research Project (JPJSBP1 2019833) and KAKENHI No. 18K05048, JSPS. This work was partly supported by NRF Grants (NRF-2019K2A9A2A08000160, NRF-2018R1D1A1B07046676). AY acknowledges the support from IQCE Research Fellowship for Senior Fellow.

Data availability statement

The data that support the findings of this study are available upon reasonable request from the authors.

Appendix

In this appendix, when the nondipole effects are appreciable, it is explained that the partial cross-sections are not directly obtainable from the photoelectron intensity measured at the magic angle in the backscattering geometry. In the coordinate system with the z-axis pointing in the photon propagation direction and the x-axis parallel to the polarization vector, the differential cross-section for photoionization for randomly oriented atoms is given by the following [17]:

$$\frac{d\sigma}{d\Omega}(\theta,\phi) = \frac{\sigma}{4\pi}\left[1 - \frac{\beta}{2}\left(P_2(\cos\,\theta) - \frac{3}{2}\tilde{S}_1\,\cos\,2\phi\sin^2\theta\right) + \delta\,\cos\,\theta + \frac{1}{2}\gamma(1+\tilde{S}_1\,\cos\,2\phi)\cos\,\theta\sin^2\theta\right]. \tag{A.1}$$

For the backscattering magic angle CMA, $\theta_{\rm mag} = 125.3^\circ$ is inserted in equation (A.1) as follows:

$$\frac{d\sigma}{d\Omega}(\theta_{\rm mag},\phi) = \frac{\sigma}{4\pi}\left[1 - \frac{\delta}{\sqrt{3}} - \frac{\gamma}{3\sqrt{3}} + \left(\frac{\beta}{2} - \frac{\gamma}{3\sqrt{3}}\right)\tilde{S}_1\,\cos\,2\phi\right]. \tag{A.2}$$

CMA accepts all electrons around the ϕ-direction, and thus a ϕ-integration in equation (A.2) is applied:

$$\int_0^{2\pi}\frac{d\sigma}{d\Omega}(\theta_{\rm mag},\phi)d\phi = \frac{\sigma}{4\pi}\left[1 - \frac{\delta}{\sqrt{3}} - \frac{\gamma}{3\sqrt{3}}\right]2\pi. \tag{A.3}$$

Under these conditions, the backscattering magic angle CMA provides an intensity $I_{\rm exp}(\theta_{\rm mag})$ of detected electrons, which is related to the partial cross-section σ:

$$I_{\rm exp}(\theta_{\rm mag}) \sim \int_0^{2\pi}\frac{d\sigma}{d\Omega}(\theta_{\rm mag},\phi)d\phi = \frac{\sigma}{2}\left[1 - \frac{1}{3\sqrt{3}}(3\delta+\gamma)\right]. \tag{A.4}$$

From this result of equation (A.4), equation (6) in the study by Kivimäki *et al* [5] is corrected through the following:

$$\sigma_{\rm 3d}\left[1 - \frac{1}{3\sqrt{3}}(3\delta+\gamma)_{\rm 3d}\right] = \frac{I^{\rm 3d}_{\rm exp}(\theta_{\rm mag})}{I^{\rm Ne2p}_{\rm exp}(\theta_{\rm mag})}\sigma_{\rm Ne2p}\left[1 - \frac{1}{3\sqrt{3}}(3\delta+\gamma)_{\rm Ne2p}\right], \tag{A.5}$$

where $\sigma_{\rm 3d}$ and $\sigma_{\rm Ne2p}$ represent the Xe 3d and Ne 2p partial photoionization cross-sections, respectively, and $I^{\rm 3d}_{\rm exp}(\theta_{\rm mag})$ and $I^{\rm Ne2p}_{\rm exp}(\theta_{\rm mag})$ express the Xe 3d and Ne 2p photo-line intensities measured by the CMA. On the one hand, $(3\delta+\gamma)_{3d} = 0.1$ at 750 eV, as described in section 2, and thus one can approximate by $\sigma_{\rm 3d}\left[1 - \frac{1}{3\sqrt{3}}(3\delta+\gamma)_{\rm 3d}\right] \approx \sigma_{\rm 3d}$. On the other hand, the nondipole effect is appreciable for Ne 2p photoionization, that is, $(3\delta+\gamma) = 0.7$ at 750 eV [35]. Thus, $\sigma_{\rm Ne2p}\left[1 - \frac{1}{3\sqrt{3}}(3\delta+\gamma)_{\rm Ne2p}\right]$ results in 0.86 $\sigma_{\rm Ne2p}$. Finally, equation (A.5) is rewritten as follows:

$$\sigma_{\rm 3d} = \frac{I^{\rm 3d}_{\rm exp}(\theta_{\rm mag})}{I^{\rm Ne2p}_{\rm exp}({\rm mag})} \times 0.86\sigma_{\rm Ne2p}. \tag{A.6}$$

As a consequence, we reached the conclusion that Kivimäki *et al* [5] overestimated the Xe 3d cross-section by 16%, because they overlooked this factor of 0.86 in equation (A.6).

ORCID iDs

S Minemoto https://orcid.org/0000-0001-5868-823X
T Majima https://orcid.org/0000-0003-2804-1915
T Mizuno https://orcid.org/0000-0001-6847-8412

References

[1] Becker U, Shirley D A 1996 *VUV and Soft X-Ray Photoionization* ed U Becker *et al* (New York: Plenum)
[2] Becker U and Shirley D A chapter 5 in reference [1].
[3] Walker T E H and Waber J T 1974 *J. Phys. B: At. Mol. Phys.* **7** 674
[4] Becker U, Kerkhoff H G, Kupsch M, Langer B, Szostak D and Wehlitz R 1987 *J. Phys. Colloq.* **48** C9-497
[5] Kivimäki A, Hergenhahn U, Kempgens B, Hentges R, Piancastelli M N, Maier K, Rüdel A, Tulkki J J and Bradshaw A M 2000 *Phys. Rev.* A **63** 012716
[6] Toffoli D, Stener M and Decleva P 2002 *J. Phys. B: At. Mol. Phys.* **35** 1275
[7] Radojević V, Davidović D M and Amusia M Y 2003 *Phys. Rev.* A **67** 022719
[8] Siegbahn K *et al* 1969 *ESCA Applied Free Molecules* (Amsterdam: North-Holland)
[9] This project was conducted at the SSS-XES/XAS beamline of Pohang Accelerator Laboratory (PAL)-XFEL with the approval of PAL (Proposal Number; 2019-1st-SSS-007).
[10] Geloni G, Kocharyan V and Saldin E 2015 *Opt. Commun.* **356** 435
[11] Nakajima K *et al* 2015 *Sci. Rep.* **5** 14065
[12] Park S H, Yoon J, Kim C, Hwang C, Kim D-H, Lee S-H and Kwon S 2019 *J. Synchrotron Radiat.* **26** 1031
[13] Even U, Jortner J, Noy D, Lavie N and Cossart-Magos C 2000 *J. Chem. Phys.* **112** 8068
[14] Minemoto S *et al* 2016 *Sci. Rep.* **6** 38654
[15] Minemoto S *et al* 2018 *J. Phys. Commun.* **2** 115015
[16] Cooper J W 1990 *Phys. Rev.* A **42** 6942
[17] Bechler A and Pratt R H 1990 *Phys. Rev.* A **42** 6400
[18] Cooper J W 1993 *Phys. Rev.* A **47** 1841
[19] Shaw P S, Arp U and Southworth S H 1996 *Phys. Rev.* A **54** 1463
[20] Trzhaskovskaya M B, Nefedov V I and Yarzhemsky V G 2001 At *At. Data Nucl. Data Tables* **77** 97
[21] Hosaka K, Adachi J, Golovin A V, Takahashi M, Teramoto T, Watanabe N, Yagishita A, Semenov S K and Cherepkov N A 2006 *J. Phys. B: At. Mol. Opt. Phys.* **39** L25
[22] Takahashi M, Cave J P and Eland J H D 2000 *Rev. Sci. Instrum.* **71** 1337
[23] Winterhalter J, Maier D, Honerkamp J, Schyja V and Helm H 1999 *J. Chem. Phys.* **110** 11187
[24] van Leeuwen R and Baerends E J 1994 *Phys. Rev.* A **49** 2421
[25] Johnson W R and Lin C D 1979 *Phys. Rev.* A **20** 964
[26] Fischer C F and Parpia F A 1993 *Phys. Lett.* A **179** 198
[27] Schmidt V 1997 *Electron Spectrometry of Atoms Using Synchrotron Radiation* (Cambridge: Cambridge University Press)
[28] Kennedy D J and Manson S T 1972 *Phys. Rev.* A **5** 227
[29] Kutzner M, Radojević V and Kelly H P 1989 *Phys. Rev.* A **40** 5052
[30] Amusia M Y, Baltenkov A S and Chernysheva L V 2007 *Phys. Rev.* A **75** 043201
[31] Arp U, Iemura K, Kutluk G, Nagata T, Yagi S and Yagishita A 1999 *J. Phys. B: At. Mol. Opt. Phys.* **32** 1295
[32] Lindle D W, Ferrett T A, Heimann P A and Shirley D A 1988 *Phys. Rev.* A **37** 3808
[33] Schmidt V 1992 *Rep. Prog. Phys.* **55** 1483 and references therein
[34] Becker U, Szostak D, Kerkhoff H G, Kupsch M, Langer B, Wehlitz R, Yagishita A and Hayaishi T 1989 *Phys. Rev.* A **39** 3902
[35] Hemmers O *et al* 1997 *J. Phys. B: At. Mol. Opt. Phys.* **30** L727
[36] Keski-Rahkonen O and Krause M O 1974 *At. Data Nucl. Data Tables* **14** 139